J Mater Sci: Mater Electron (2025) 36:187

The influence of annealing temperature on the gas sensing properties of multifunctional hematite (α-Fe_2O_3) films

Fatma Sarf[1], Irmak Karaduman Er[2,*], Emin Yakar[3], and Selim Acar[4]

[1] *Çan Vocational School, Çanakkale Onsekiz Mart University, Çanakkale, Turkey*
[2] *Department of Medical Services and Techniques, Eldivan Medical Services Vocational School, Çankırı Karatekin University, Çankırı, Turkey*
[3] *Department of Materials Science and Engineering, Faculty of Engineering, Çanakkaleanakkale Onsekiz Mart University, Çanakkale, Turkey*
[4] *Department of Physics, Faculty of Science, Gazi University, 06510 Ankara, Turkey*

Received: 8 August 2024
Accepted: 7 January 2025
Published online:
22 January 2025

ABSTRACT

In this study, hematite (α-Fe_2O_3) were prepared using direct solution spin coating and the changes of some physical properties with annealing temperature (400, 500 and 600 °C) for 2 h were investigated. The sensors annealed at 400 °C, 500 °C and 600°C are referred to as F400, F500 and F600 respectively. The X-ray diffraction patterns of the prepared samples confirm the polycrystalline nature of the rhombohedral crystal structure of hematite (α-Fe_2O_3). The surface roughness parameters (SA-SQ) of the α-Fe_2O_3 films decreased drastically with increasing annealing temperature from 400 to 600 °C (57.47–68.08/13.63–17.13). The direct optical band gap values were estimated from absorption measurements and ranged from 2.77 to 2.52 eV. The electrical resistivity measurement at room temperature of the samples decreased with increasing annealing temperature from 400 to 600 °C. The response of the CO sensor of F400, F500 and F600 was found at 180 °C. The response to 1 ppm CO gas was calculated to be 1.45%, 8% and 10% for F400, F500 and F600 respectively. The wettability test of the samples showed a water contact angle (WCA) of less than 90°, demonstrating the hydrophilic surface especially for the samples annealed at 500 °C.

1 Introduction

Carbon monoxide (CO) is a colorless and odorless gas that causes headaches, nausea, weakness, fatigue and dizziness. It is a blood-poisoning gas. By blocking the enzyme cytochrome oxidase in the body, it significantly inhibits the blood's ability to use and transport oxygen [1]. It prevents the transfer of oxygen between cells and therefore has a negative effect on organs that require large amounts of oxygen, such as the brain, heart and liver. It leads to paralysis, respiratory arrest and cardiac arrest [2]. Research on sensors

Address correspondence to E-mail: karaduman.irmak@gmail.com

https://doi.org/10.1007/s10854-025-14244-w

with fast response and feedback time that can detect low concentrations of CO gas is accelerating.

Gas sensors are electronic devices capable of detecting various substances in the environment in gaseous form (combustible or toxic gases, humidity, volatile organic substances) and calculating their concentrations. Gas sensors are able to regulate the presence and concentration of gases in the environment and control their functions such as monitoring and measurement. Thanks to these characteristics, they have become one of the most fundamental and effective elements to prevent the damage that developing technology and industry is causing to nature and people. For this reason, the importance of studies carried out specifically for gas sensors has increased and has been further accelerated by the integration of technological developments in this process. The sensitivity and selectivity of metal oxides for certain analytes can be increased by designing the material composition, adding additives or modifying their surface properties. Metal oxide semiconductors outperform other sensors in terms of performance due to their special structures and exceptional physical and chemical properties.

The oxygenated components of iron [ferrous oxide, FeO; ferric oxide, Fe_2O_3; and ferrosoferric oxide, or ferroferric oxide, Fe_3O_4] are remarkable due to their high chemical stability, highly developed magnetic structures, relatively low toxicity, and abundance in nature [3]. They primarily obtained from the minerals hematite (Fe_2O_3) and magnetite (Fe_3O_4). The minerals taconite, limonite ($FeO(OH){\cdot}nH_2O$) and siderite ($FeCO_3$) are other important sources. Latin ferrum. Among them, hematite exhibits a hexagonal corundum structure in which the O^{2-} ions are arranged in a hexagonal closed packing, while two-thirds of the octahedral sites between the oxygen ions are occupied by Fe^{3+} ions [4]. Scientists investigated the magnetic properties of hematite structures for ultra-high magnetic storage and magneto-optical sensors due to the favourable interactions within and between the particles [5]. However, in recent years, hematite has served as an advanced material in many reports with its chemical stability compared to γ-Fe_2O_3, its narrow band gap (~ 2.1 eV for massive hematite) suitable for light absorption, its excellent sensitivity towards poisonous gases, its occurrence in nature, and its low toxicity [6, 7].

With the increasing demand and cost, the design of semiconductor materials suitable for many different applications has become very important in recent years. As a promising functional material, hematite has been used in various applications such as gas sensors [8], photo-electrochemistry [PEC] [9], optoelectronic devices [10], and photo-oxidation of water [11]. However, hematite still has some problems, such as low mobility and a tendency to agglomerate [12]. On the other hand, solution-fabricated thin films with a thickness of several hundred nanometers are usually outstanding, but some critical issues pose challenges for commercialization, such as stability and scalability, etc. [13]. Thick films are scalable by reducing interfacial tension and are suitable for large-scale coating fabrication. In addition, a thicker film with a lower surface-to-volume ratio tends to be more resistant to environmental factors such as moisture and oxygen, thus improving chemical robustness [14]. Unfortunately, even though these problems are reduced with a thicker micrometer-scale film, the performance of the devices is lower with thick films than with thin films. Although the mechanism is difficult to understand, the main limiting factor is the short carrier lifetime as a result of defect traps in the thick film [15, 16]. Annealing hematite films in an air environment is an approach that is very commonly used in the literature and can be summarized as follows: when the annealing temperature is increased from 400 to 600 °C with a residence time of 4 h, for example, amorphous iron oxide is converted into hematite and the average particle size increases from 65 to 95 nm [17].

The enlargement of grains by the migration of surface atoms, which contributes to the incorporation of iron and oxygen atoms into the lattice regions, has been demonstrated [18]. In another similar study on hematite thin films, a post-annealing process was carried out with three different heating rates at 350 °C for 15 min, which induces oxygen vacancies and the formation of hydroxyl groups on the surface [19]. In this context, the main technological challenge is to control the physical properties, all of which affect the properties of the synthesized material and determine its field of application. In this work, the influence of annealing temperature on the physical properties and multifunctionality of hematite films were investigated. The hematite films were prepared by direct solution spin coating and the annealing temperature was set at 400, 500 and 600 °C for 2 h. These samples were annealed at different temperatures and the effect of annealing on the gas detection effect was discussed.

2 Materials and methods

Fe_2O_3 films were prepared by direct solution spin coating. FTO (fluorine-doped tin oxide) material was used as a substrate, which was cut into 20 mm × 20 mm pieces. FTO glass is a metal oxide material used to fabricate for thin-film photovoltaics, organic photovoltaics, gas sensors, diodes, amorphous silicon, cadmium telluride, and hybrid perovskites. It was then cleaned in an ultrasonic bath with detergent, ethanol and *n*-hexane for 10 min. The cleaned substrates were dried in an oven at 80 °C. All solvents and chemicals are of analytical grade so that further purification is not required (≥ 99%). Ferrous sulfate heptahydrate, ethylene glycol, 2-proponal and HCl were used as precursor, solvent and stabilizer, respectively. First, 0.278 g of iron precursor was dissolved in 2.5 ml of ethylene glycol and 2.5 ml of 2-proponal solution at room temperature and HCl was added dropwise until the pH of the solution was 0.9 (in strongly acidic medium). The solution was then stirred in a magnetic heating mixer at a constant temperature of 55 °C for 2 h. The aged sol was spun at 2500 rpm for 20 s at a ramp rate of 50 rpm/s onto FTO substrates. The coated films were air dried at 150 °C for 20 min. The coating-drying process was repeated 4 times. Finally, the synthesized films were annealed at 400, 500 and 600 °C for 2 h in an oven without gas emission. An adhesive tape test was carried out on the synthesized films. It was found that the films did not detach from the substrate and adhered well to the substrate.

Powder XRD measurement of samples was performed using a Rigaku SmartLab diffractometer with CuK_{α} (1.5406 Å) radiation operating at 40 mA and 45 kV between 2θ = 10°–80° range. 3-D surface topographies of the samples were studied in non-contact mode with using an atomic force microscopy (Witec alpha 300 RA). Film thickness of the samples detected by OPT-S9000 spectroscopic ellipsometer along a 2000 μm line. The optical absorbance $\alpha(\lambda)$ of the samples were recorded by Schimadzu UV 3100 double-beam spectrophotometer, between 275 and 1100 nm range. With the help of a micro syringe, distilled water drops with a volume of 5 μl were measured using a contact angle goniometer. Screenshots of the drops were analyzed with standard software to calculate the contact angles.

Gas sensor measurement system consists of Keithley 2400, a modified vacuum cell for gas measurements, LakeShore temperature controller, MKS Flow Controllers (MFC), impedance measurement device, high purity dry air, CO gas and vacuum pump. Sensor cell consists of the sample holder, gas valves that provide inlet and outlet of the target gas, and BNC connectors for the sensor's Keithley 2400 device. There are semiconductor sensor connection terminals to detect the temperature of the sensor, connection terminals of the Lakeshore 325 temperature controller to heat the material when necessary, and also a sensor cell.

Gas detection measurements were made using the Keithley 2400 device. First, the sensors were placed in the measurement cell. Sensors placed in the cell using the Lekeshore 325 temperature controller were kept in the determined constant temperature environment. Gas flow to the sensor surface was achieved using (MKS) gas pressure and flow controllers. Using the flow controller, the desired target gas concentrations were adjusted and gas measurements were made. The samples were coded F400, F500 and F600 for α-Fe_2O_3/400, α- e_2O_3/500 and α-Fe_2O_3/600, respectively.

3 Results and discussion

Figure 1 shows the XRD patterns of the prepared samples. The XRD peaks have an expanding character, revealing the nano-property of the samples. The crystal planes were determined using a standard PDF card. The prominent diffraction peaks (012), (104), (110), (113), (024), (116), (214) and (300) are assigned to the diffraction planes of the rhombohedral α-Fe_2O_3 structure (JCPDS Card No.: 79-0007) [20]. No traces

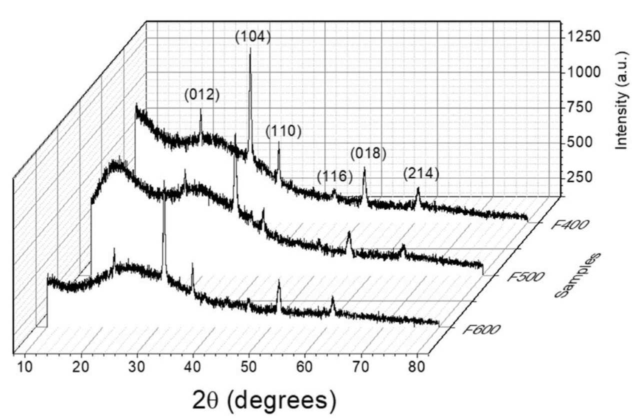

Fig. 1 The X-ray patterns of produced α-Fe_2O_3 samples

of secondary phases such as FeOOH, Fe_3O_4 and FeO were detected. This indicates the purity of the synthesized samples, which consist of a single α-Fe_2O_3 phase. the (104) indexed peak is the preferred orientation for all samples. With increasing annealing temperature from 400 to 600 °C, a slight shift of the 2θ angle of the (104) preferred orientation to the left was observed with the change of strain in the substrate/film layer and a strong shrinkage of the half-peak width. This indicates that the crystal quality is improved by the annealing process, which means that the transformation of the amorphous precursor films into hematite, assisted by annealing, was carried out in all thicknesses. Relative increase was observed in average grain size which measured by X-ray diffractometer with increasing annealing temperature from 400 to 600 °C. With using cathodic electrodeposition method, nanostructured hematite thin films exhibited increasing particle size with increasing annealing temperature from 400 to 600 °C, the results are consistent with literature [20]. Increasing annealing temperature from 400 to 600 °C supports diffusion of atoms at the grain boundaries and growth of crystallites [21]. The crystallize size which calculated by the Scherer equation [21] were calculated 31 nm, 85 nm and 110 nm for F400, F500 and F600, respectively.

Figures 2 and 3 give the Halder–Wagner and Wagner–Aqua analyses of produced α-Fe_2O_3 samples, respectively. Halder–Wagner introduced an empirical model to calculate lattice strain $\varepsilon_{H\text{-}W}$ and mean crystallite size $D_{H\text{-}W}$, as given in Eq. (1) [22];

$$\left(\frac{\beta}{\tan\theta}\right)^2 = \left(\frac{k\lambda}{D_{(H-W)}}\right)\cdot\left(\frac{\beta}{\tan\theta\sin\theta}\right) + 16\varepsilon^2_{(H-W)} \quad (1)$$

The Wagner–Agua method is also an analytical technique that can be used to simultaneously extract the mean crystallite size $D_{(W\text{-}A)}$ and lattice strain $\varepsilon_{(W\text{-}A)}$ of a sample, as illustrated in Eq. (2) [22];

$$(\beta\cos\theta)^2 = (4\sin\theta\cdot\varepsilon_{(W-A)})^2 + \left(\frac{k\lambda}{D_{(W-A)}}\right)^2. \quad (2)$$

Table 1 gives the Crystalline size and lattice strain of the produced samples which were analyzed from three different methods (Debye-Scherrer, Wagner–Agua and Halder–Wagner) [23–27]. If you examine the tables, you can see that the four methods harmonise with each other.

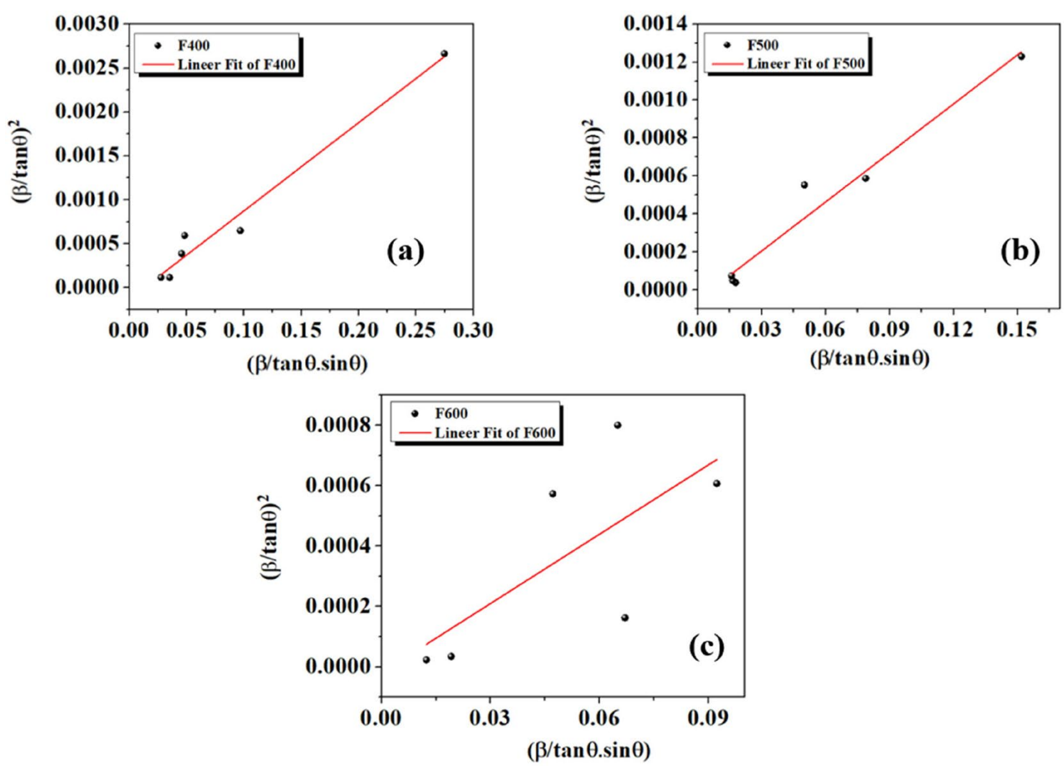

Fig.2 Halder–Wagner analyses of produced α-Fe_2O_3 samples

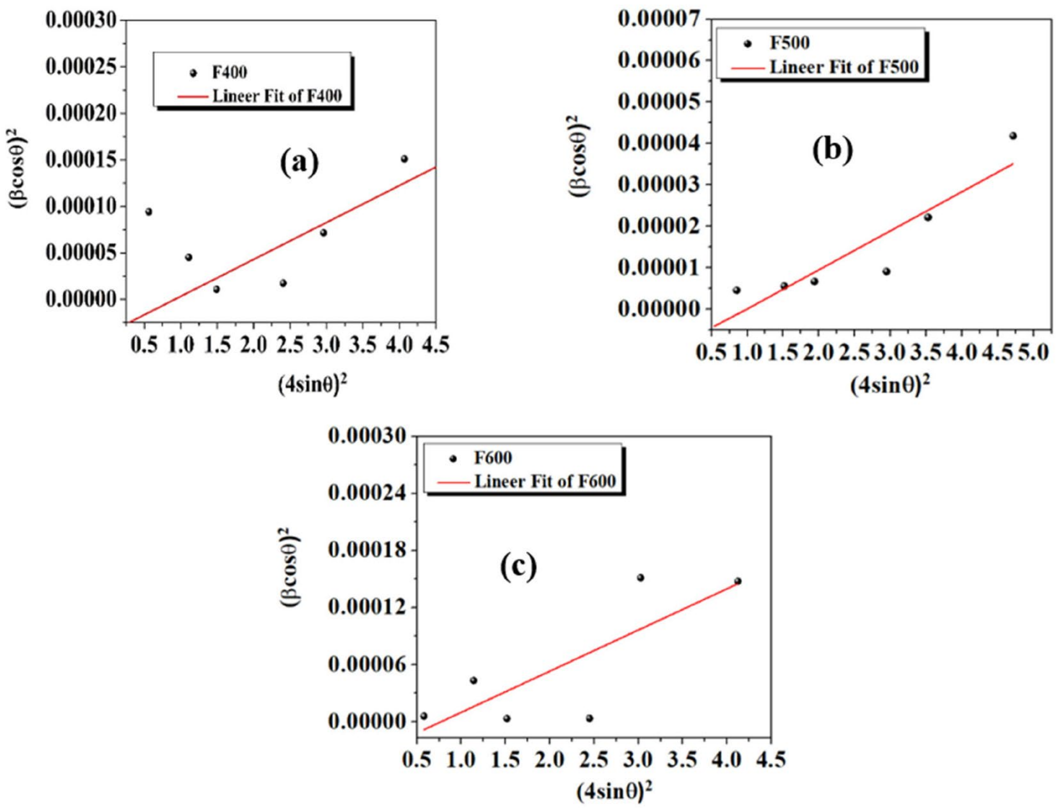

Fig. 3 Wagner–Aqua analyses of produced α-Fe_2O_3 samples

Table 1 The Crystalline size and lattice strain of the produced samples which were analyzed from three different methods (Debye–Scherrer, Wagner–Agua and Halder–Wagner)

Samples	Crystalline Size (nm)			Lattice Strain		
	Debye–Scherrer	Wagner–Aqua	Halder–Wagner	Debye–Scherrer	Wagner–Aqua	Halder–Wagner
F400	77	96	95	0.0015	0.00078	0.0008
F500	66	81	83	0.0018	0.00095	0.0009
F600	46	57	65	0.0027	0.00115	0.0017

Figure 4 shows the topography of the α-Fe_2O_3 surfaces on the FTO substrate obtained from AFM measurements in non-contact mode (0.9 × 0.9 μm). Islands separated by cracks were observed in annealed samples at 400 °C due to low precursor solubility in heavy acidic medium at relative low temperature of 400 °C. The formation of tooth-like structures was observed during annealing at 500 °C, and the dimensions of the tooth-like structures decreased during annealing at 600 °C. This is due to the nucleation and coalescence phenomena that occur during the annealing processes [28–31].

UV–vis absorption study of films synthesized at various annealing temperatures shown in Fig. 5. With increasing annealing temperature, the absorption edge has shifted to lower wavelengths which implies to blue shift. Strong absorption edge of the samples is located at 424 nm (2.92 eV), 365 nm (3.39 eV) and 351 nm (3.51 eV) for annealing at 400, 500 and 600 °C, respectively. In Fig. 5c, there are two absorption edges, as strong and weak, observed for annealed samples at 600 °C. Weak absorption peak at ~ 530 nm (2.33 eV) attributed to ligand-field (LF) *d*–*d* transitions by reorientation of electrons from one Fe 3d orbital to another on the same

Fig. 4 3-D and 2-D AFM images of F400 (**a**), F500 (**b**) and F600 (**c**)

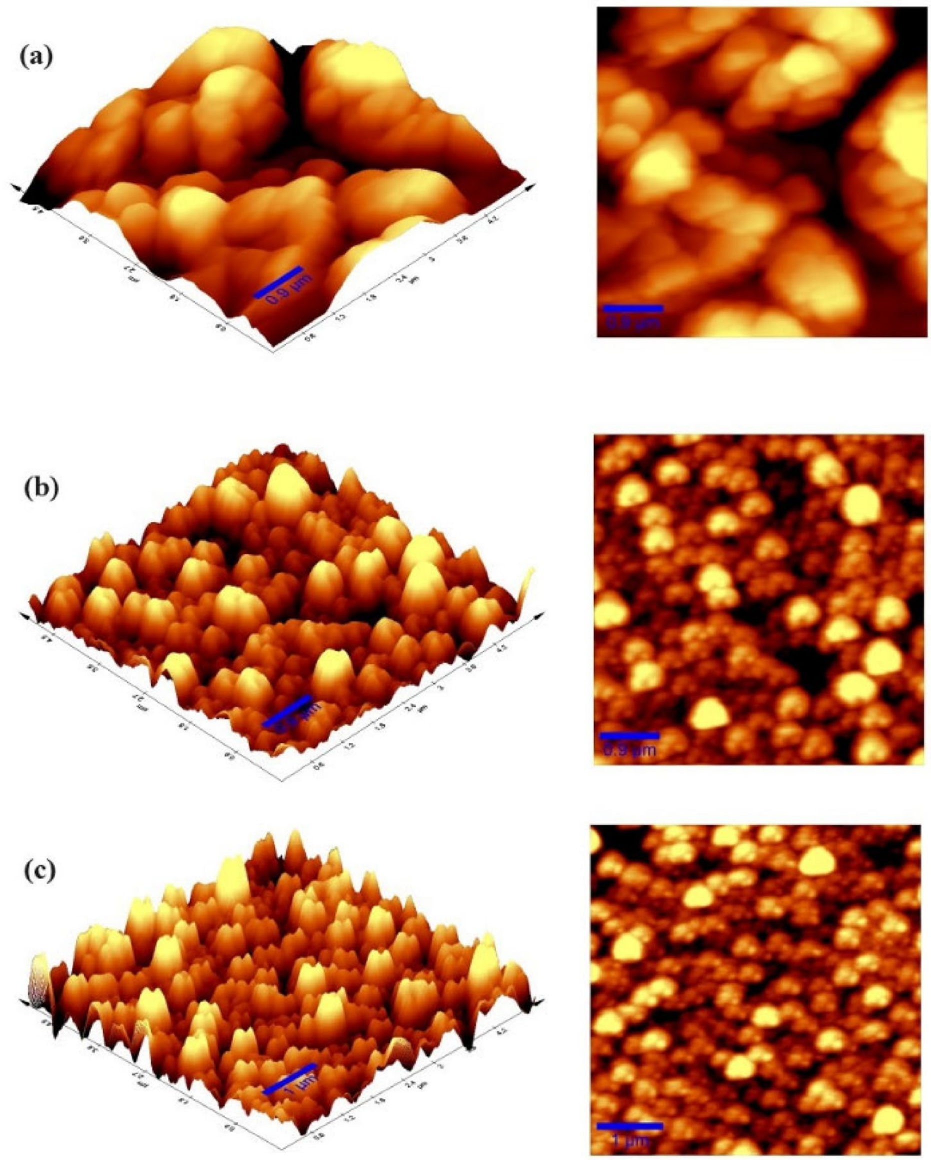

Fe site or due to simultaneous LF transitions on adjacent Fe sites [32, 33]. The observed optical absorption edges of nanostructured hematite films may be due to the variations of annealing temperature.

Band gap is one of the basic parameters of a semiconductor, and its correct determination is essential to optimize its performance in various applications. In general, the optical band gap energy values were obtained using the Tauc plot, as shown by Eq.3. [34];

$$((\alpha h\nu)^{\frac{1}{n}} = A(h\nu - E_g)), \tag{3}$$

where α is the absorption coefficient (cm^{-1}), h is the photon energy (eV), A is the material-dependent constant, E_g stands for optical band gap energy, and n takes 0.5 and 2.0 values, corresponding to direct and indirect transitions, respectively. The intercepts of the extrapolated linear portions of these plots to $h\nu = 0$ represent E_g Values of the films. It has been determined that the obtained optical band values are 2.77 eV, 2.52 eV and 2.71 eV for annealed samples at 400, 500 and 600 °C, respectively, as seen in Fig. 6. Band gap of produced thick films are higher than the hematite thin film studies (~ 2.1–2.3 eV) in the literature which may be due to the various lattice-associated atomic interaction phenomena that come into play from its ionic crystalline lattice nature [35].

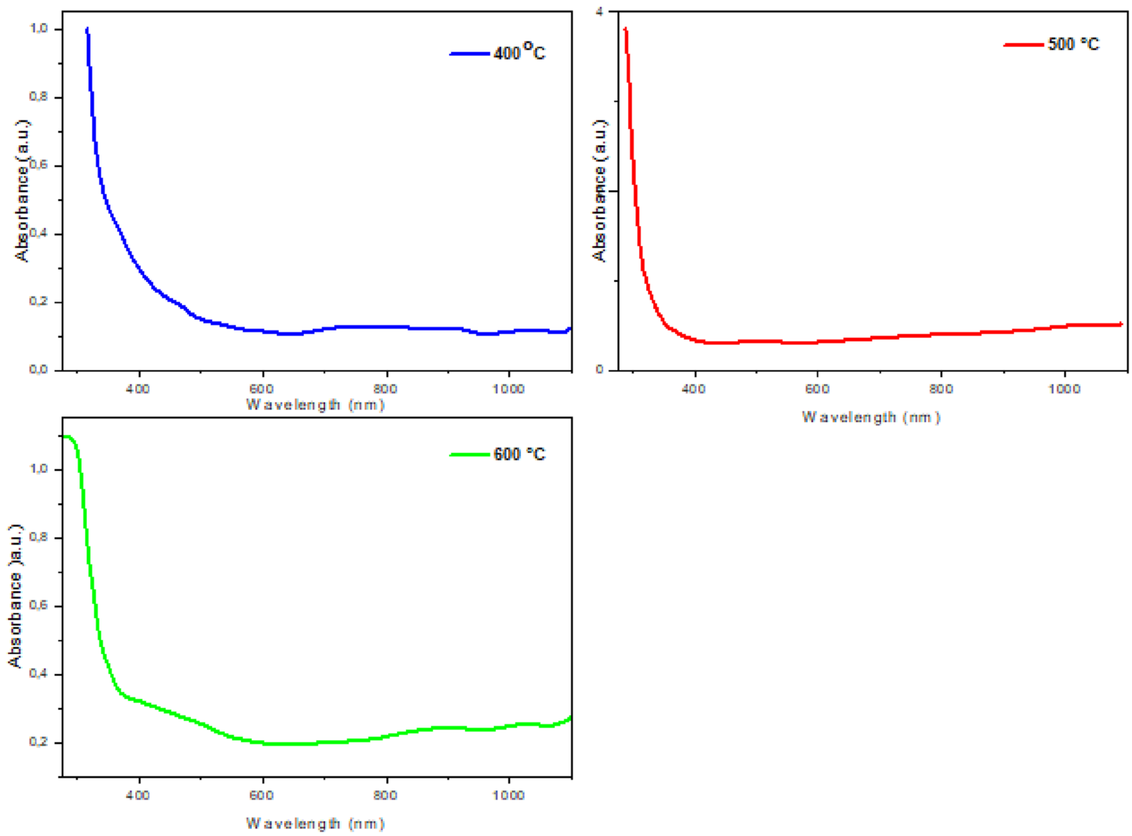

Fig. 5 UV–Vis spectrum of α-Fe_2O_3 films for F400 (a), F500 (b) and F600 (c)

In addition, the reason for the small decrease in the E_g value at 500 °C can be associated with the extent of non-stoichiometry of the deposited layers. In addition, when it comes to the investigation of the optimum annealing temperature, it is seen that 600 °C is the optimum annealing temperature. The band gap variation differs entirely in thin films compared to thick material. In the investigation of the thick films, the band gap values are completely different from the thin films. A perturbation is seen in the energy gap. This situation can be associated with the Madelung energy due to charge–charge interactions in the system, the delocalization energy due to electron sharing between atoms and the internal energy due to the filling of atomic orbital/intra-atomic electron–electron interactions [36]. However, as shown in Fig. 6, since the definition of the baseline is usually not well defined, a straight line from the lowest value in the Tauc graph or a linear alignment to the low-energy part of the Tauc graph is preferred and causes deviation for device applications, as explained by Zhong et al. [37].

Figure 7 exhibited the resistance values for α-Fe_2O_3 films for different annealing temperatures. The resistances were calculated as 2198, 902 and 386 kΩ for F400, F500 and F600, respectively. High resistivity (~ 10^2 Ω) values can be used as an indicator of the purity of hematite films and increased with annealing (~ 10^5 Ω), as explained by Glasscock et al. [38]. The results obtained show that the mobility is due to the structural defects of the ionized iron atoms and the scattering at these defects as well as the scattering at the grain boundaries. According to the literature, the performance of hematite thin films can be enhanced by various treatments such as optics, light, humidity and pressure to improve the conductivity properties [39]. According to Chakraborty et al., annealing process decreased the ionization energy of impurity conduction due to decreased trap levels and increased conductivity with increased width of necked particles

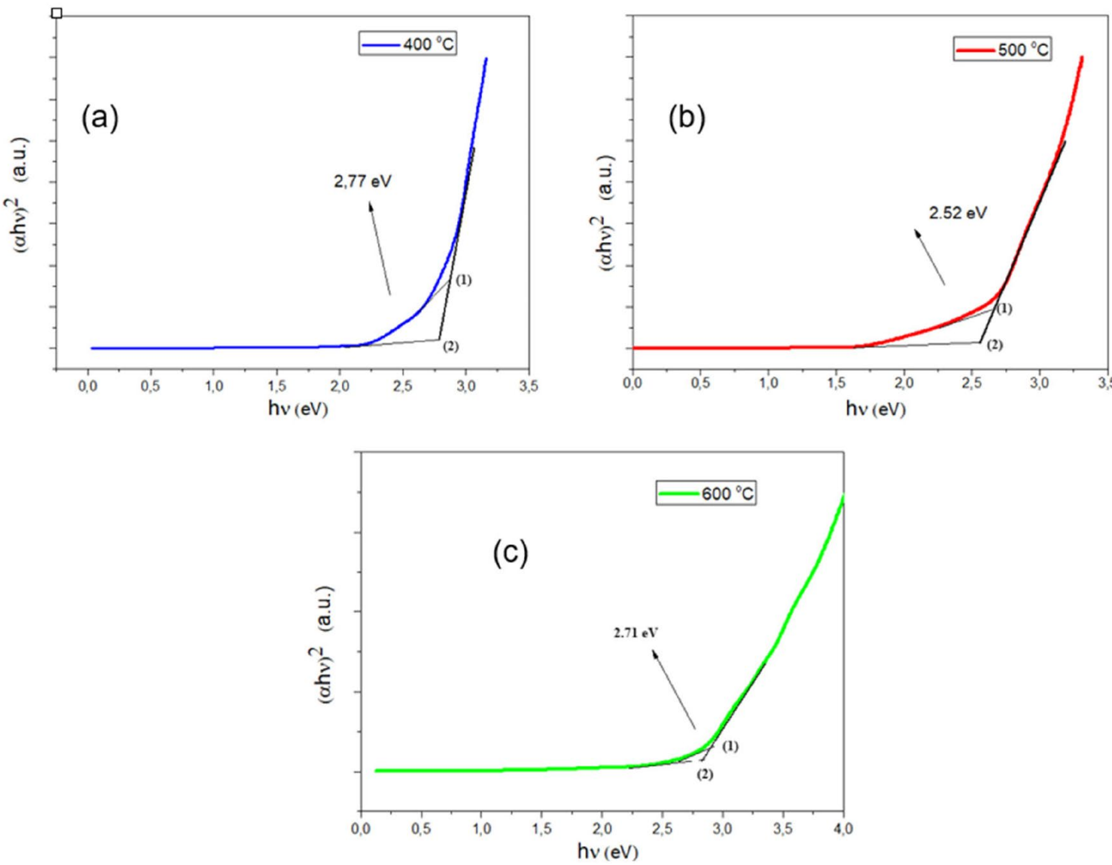

Fig. 6 Tauc plots for α-Fe_2O_3/400 (**a**), α-Fe_2O_3/500 (**b**) and α-Fe_2O_3/600 (**c**) samples (The effect of localized defect absorption around the bandgap and $((\alpha h\upsilon)^2$ are designated by (1) and (2))

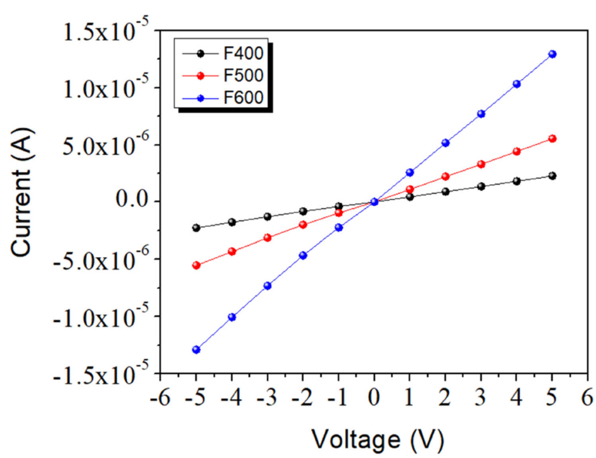

Fig. 7 The resistance values for α-Fe_2O_3 films for different annealing temperatures 400 °C, 500 °C and 600 °C

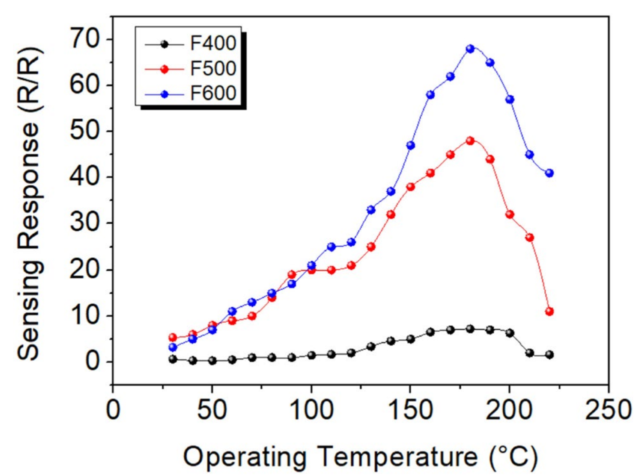

Fig. 8 The gas sensing measurements as a function of operating temperature

respectively followed by increase in charge transportation for hematite thin films with necked particle size ranging from 17 to 23 nm [40].

CO is a toxic, odorless and colorless gas type. Improving the gas sensing sensitivity and lowering the working temperature are the critical issues for the practical application of gas sensors. The operating temperature was found to be 180 °C. However, the F600 sensor exhibited a 5% response to CO gas at room temperature. It is seen as an acceptable response when investigating the literature studies [41–43]. As seen from Fig. 8, an increase in response was observed as the temperature increased. Later, when the operating temperature of 180 °C was exceeded, decreases in sensor sensitivities began to be observed. The relationship between response and temperature can be explained by its dependence on the amount of adsorbed oxygen atoms.

However, surface content, factors that accelerate adsorption, chemical decomposition and other reactions also change depending on temperature [44]. With the increase in temperature, the electrons in the structure gain energy and current conduction occurs. Therefore, an increase in response is observed as the temperature increases. The main reason for the lack of response below a certain temperature is electrical instability. The reason for electrical instability is the mixed oxide phases in the environment and, accordingly, the number of carrier electrons on the surface is changed by the molecular oxygen type that is chemically adsorbed under the effect of the operating temperature. The instability disappears with the increase in temperature and the decrease in the mixed oxide phases [45, 46]. However, if the temperature is too high, the reaction may occur too quickly and the diffusion of gas molecules to the surface will not be sufficient. This is because the reaction decreases when the desorption rate exceeds the adsorption rate of the gas molecules from the sensor surface at high temperatures.

After the operating temperature was set at 180 °C, dynamic gas standard measurements were made from 1 ppm to 9 ppm with a step of 2 ppm at this operating temperature. Fig. 9 gives the dynamic CO gas sensing for F400 (a), F500 (b) and F600 (c). Examination of the graph revealed that samples F500 and F600 had acceptable sensitivity at a gas concentration of 1 ppm. Small shifts in the sensors' standard baseline values were observed due to the low operating temperature [47]. These values become fixed when higher temperatures are reached. However, since our goal is to obtain sensor materials that work at lower temperatures, this small shift is acceptable.

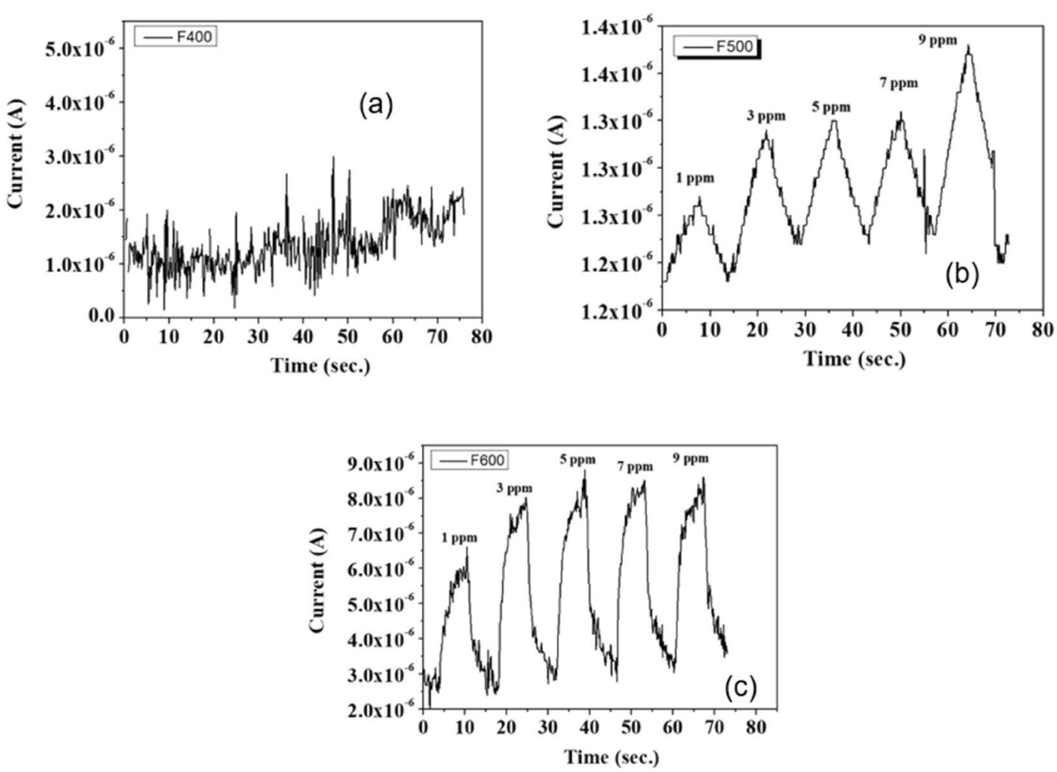

Fig. 9 The dynamic CO gas sensing for F400 (**a**), F500 (**b**) and F600 (**c**)

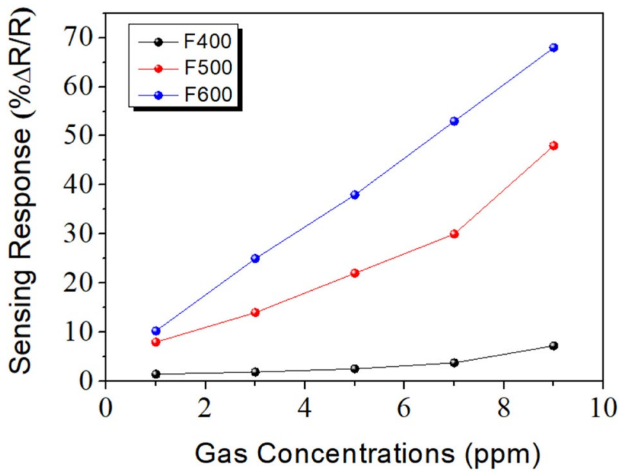

Fig. 10 The sensing response of CO gas sensing for F400, F500 and F600

In order to see and compare the sensor responses more clearly, the response-time graphs are given collectively in Fig. 10. Sensing response is calculated below Eq. (4) [48];

$$\text{Sensing response}(\%) = \frac{\Delta I}{I_{gas}} \times 100 = \frac{(I_{gas} - I_{air})}{I_{gas}} \times 100 \tag{4}$$

which is represented I_{gas} measured in air and I_{air} measured in air gas value. Fig. 10 show the CO sensing response of F400, F500 and F600 at 180 °C. The response of the 1 ppm CO gas sensing was calculated as 1.45%, 8% and 10% for F400, F500 and F600, respectively. The grain size of the material is therefore one of the key factors to control the gas sensing properties of the material [49]. Above 600 °C, the relative resistance of the device decreased rapidly with increasing annealing temperatures. In the literature, there are a lot of studies about pure or doped hematite structures which exhibited rapid response and high sensitivity towards different gases [H_2] [50], acetone [51] and *n*-butanol [52].

Gas sensors made of metal oxide (SnO_2, ZnO, In_2O_3, TiO_2, etc.) have a high electrical resistance due to the potential barrier created by the adhesion of oxygen to the material surface [53, 54]. The detection mechanism of metal oxides can be explained by the presence of oxygen vacancies on the oxide surface, which in principle can react electrically and chemically. There are therefore two types of detection reactions. (1) The electrons move away from the conduction band when the detected charged molecules attach to the empty regions, causing the conductivity to decrease. (2) On the other hand, gas molecules such as CO and H_2 react with the oxygen on the surface and return the electron (the captured electron that increases conductivity) to the conduction band. Reduction and oxidation reactions, i.e. redox reactions, take place on the surface, leading to a decrease and increase in conductivity. The expected reactions for CO gas are as follows [55];

$$2CO_{(gas)} + O^-_{2(ads)} \rightarrow 2CO_{2(gas)} + e^- 0 < T < 150°C \tag{5}$$

$$CO_{(gas)} + O^-_{(ads)} \rightarrow CO_{2(gas)} + e^- 150°C < T < 400°C \tag{6}$$

One of the basic parameters that influence the detection parameters of gas sensors is the surface area to volume ratio. The basic factors that influence the sensitivity of metal oxide semiconductor gas sensors are the depth of the depletion region (L) and the grain size (D). The ratio between the grain size and the depth of the depletion zone determines the resistance of the sensor. Reducing the grain size is one of the most important factors in improving the gas detection properties of semiconductor oxides. Accordingly, the change in electron density only takes place in the surface areas of the oxide grains. Therefore, the inner region within the depletion region does not contribute to the resistance change. If the grain size is larger than twice the Debye length, this has a negative effect on the total change in the conductivity of the material [43].

When $D < 2L$, each grain is covered by the depletion layer and participates in the charge transfer interactions with the gas molecules. Since there is no obstacle to charge transfer at the grain boundaries in this case, the energy bands of the interconnected grains are almost flat. The sensitivity of the sensor is controlled by the resistance value of the grains. The most effective situation for the sensitivity of the sensor is to control the grains.

Figure 11 give the response (**a**) and recovery (**b**) times of the F400, F500 and F600. A complete return was not observed for F500. Triangular dynamic measurements were formed. Stability occurred in the sample annealed at 600 °C and clearer times were observed in dynamic measurements When CO is injected into the sealed chamber, the response of the samples increases rapidly and gradually reaches a steady state. Then the two sensors are returned to the

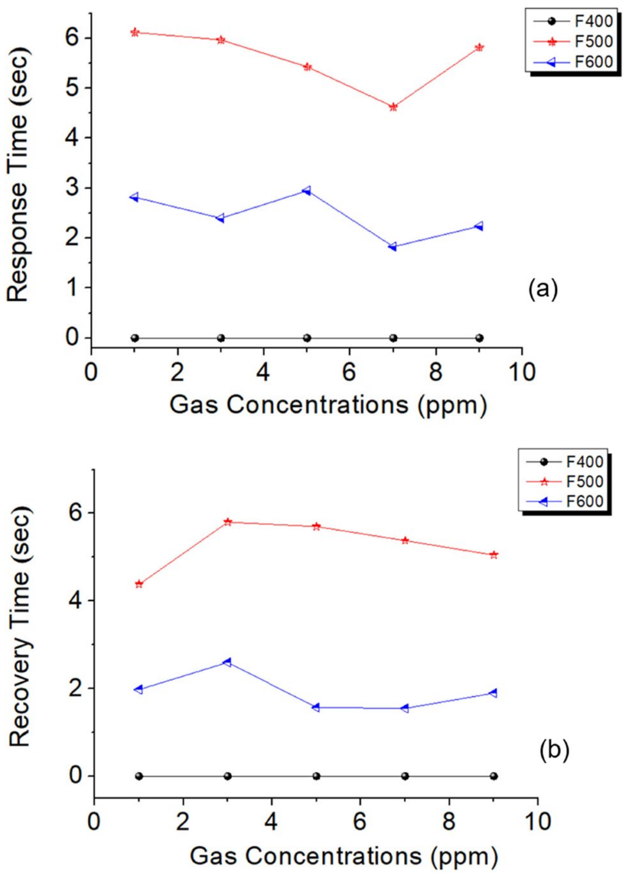

Fig. 11 **a** Response times of the F400, F500 and F600. **b** Recovery times of the F400, F500 and F600

air, the reaction rapidly returns to the initial level. In addition, the response/recovery time of the F500 and F600 samples for 9 ppm is 5.8 s/5.05 s and 2.24 s/1.19 s, respectively. The response/recovery time of F600 is shorter than that of F500, which is due to the effect of the annealing process that accelerates the redox reaction of CO [56, 57]. Response and recovery times were observed more clearly. As the F400 sample showed no response at the operating temperature of 180 °C, the response and recovery times could not be calculated. Therefore, the values in the graph were added as zero to allow a comparison of the three samples. In both films, reaction and recovery times of the order of seconds can be seen.

High stability in terms of parameters such as sensitivity, selectivity, response and recovery time are extremely important for the long-term operation of the sensor [58]. As the best gas results were obtained in the F600 sample, repeatability, selectivity and reproducibility measurements were only carried out in the F600 sample. The selectivity of a sensor is the ability to discriminate the target molecule from the interfering molecules and to show a target-specific sensor response [59, 60]. The selectivity to other interference gases was also tested by measuring the responses to 9 ppm NH_3, CO_2, NO, NO_2 ve CO at 180 °C; the plots of the results are shown in Fig. 12. Figures 13 and 14 depict the repeatability and reproducibility measurement of F600. The average of ten repeated measurements was calculated. If the sensing response value resulting from the average is close to the original value, it is emphasized that it is a sample with high repeatability. In practical applications, the long-term stability of the sensor is also an important parameter. The reproducibility measurements are performed every day with the same ppm value. If the response values obtained at the end of five days converge to the initial value, the

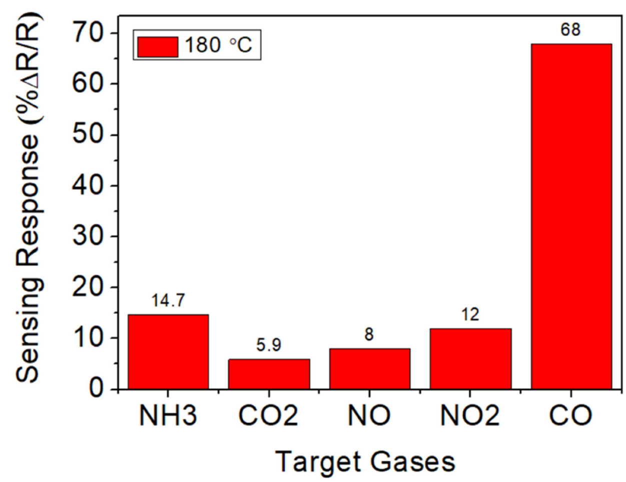

Fig. 12 The selectivity measurements of F600

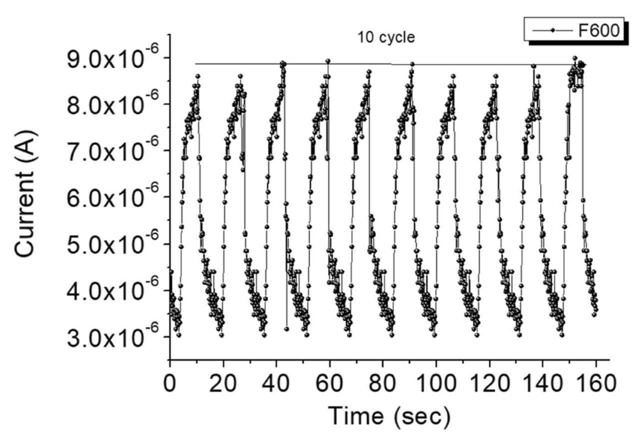

Fig. 13 The repeatability measurement of F600

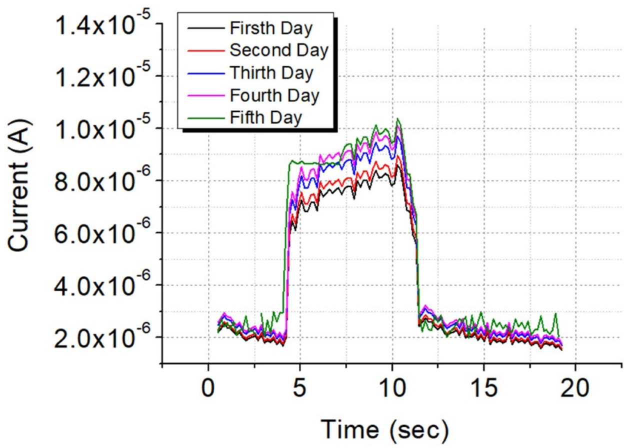

Fig. 14 The reproducibility measurement of F600

Table 2 Water droplet contact angle (WCA) measurement of α-Fe_2O_3 thin films for annealed at 400, 500 and 600 °C (The contact angle was the average of left and right angles of each drop)

Sample (°C)	WCA ± margin of error
400	72.1 ± 1.2
500	11.9 ± 1.0
600	19.8 ± 1.9

sample is considered reproducible [61–64]. The credibility of the sensor and its duration of service can be approved by the long-term stability.

High surface energy is important for the wetting of solutions, especially in manufacturing processes such as spin coating. Most solids with high surface energy cannot maintain their high-energy surface when exposed to atmospheric conditions [65]. The static contact angle for the clean and pure FTO substrate was measured to be 52.0° ± 1.9°. Fig. 15 shows images of water droplets on the surface of α- Fe_2O_3 films at different annealing temperatures. The surfaces of the samples annealed at 400 °C and 600 °C are hydrophilic. In contrast, the nature of the samples annealed at 500 °C shifted from hydrophilic (10° < ω < 90°) to superhydrophilic (ω < 10°). This indicates that the atomic composition and surface roughness, which increase the surface free energy and decrease the surface tension, have an influence on the wettability of α-Fe_2O_3 surfaces [66]. Table 2 gives the water droplet contact angle (WCA) measurement of α-Fe_2O_3 thin films for annealed at 400, 500 and 600 °C (The contact angle was the average of left and right angles of each drop).

In addition, the surface energy of films was calculated through the measured contact angle data according to the Owens–Wendt–Rabel–Kaelble (OWRK) method. The work of adhesion liquid-film has been calculated using by Equation 7 [53]:

$$\omega_{\text{ads}} = \gamma_i((\cos\theta) + 1), \quad (7)$$

where ω_{ads} is the work adhesion, θ is the contact angle and γ_L is surface free energy of liquid. The work adhesion value was found about ~ 49.62, 75.10 and 73.67 Mn m^{-1} for annealed surfaces at 400, 500 and 600 °C, respectively. These results suggest that the surfaces of the samples exhibited hydrophilic behavior when applied annealing at different temperatures. The better wettability of the F500 film, as evidenced by its lower contact angle, indicates an optimal interplay of surface roughness and surface chemistry that enables stronger interactions between the film surface and water molecules. This lower contact angle probably results from the numerous hydrophilic sites on the surface of the F500 film, which promote hydrogen bonding with the water molecules and enable better spreading of the water. From a scientific point of view, the exceptionally low contact angle of the F500

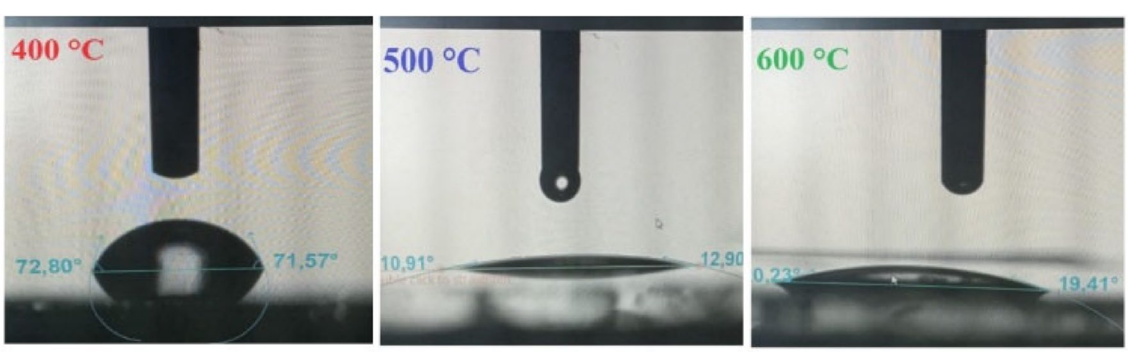

Fig. 15 Water droplet contact angle (WCA) images of α-Fe_2O_3 films for 400, 500 and 600 °C annealing temperatures

film can be attributed to an optimal microstructural arrangement that improves the hydrophilic properties. Microscale surface roughness can enhance the inherent wettability of a material, as described by the Wenzel and Cassie-Baxter models. The Wenzel model predicts that rough surfaces increase the wettability of hydrophilic materials by allowing the liquid to fully penetrate the surface irregularities, while the Cassie-Baxter model describes surfaces where air pockets are trapped in rough structures, resulting in partial wetting [67]. In more recent studies, these classical models have been extended to account for nanoscale surface modifications and further improve wettability by controlling surface energy and roughness at multiple levels [68, 69].

4 Conclusion

Polycrystalline α-Fe_2O_3 films were deposited on FTO substrates via simple direct solution spin coating. Annealing temperature effect on the structural, morphological, optical, electrical, CO gas sensing and surface wettability properties was investigated. The surface morphology of the films annealed at 500 °C exhibited tooth-like microstructure and the hydrophilic nature is most clearly seen in these samples. The response of the 9 ppm CO gas sensing was calculated as 7%, 48% and 68% for F400, F500 and F600, respectively. In addition, the response/recovery time of the F500 and F600 samples for 9 ppm is 5.8 s/5.05 s and 2.24 s/1.19 s, respectively. As a result; samples were successfully produced. The properties of CO gas detection were investigated as a function of temperature and concentration. It was found that the sensitivity decreased at high temperatures and at the same time the best response time, the best recovery of the reaction and the best stability were obtained at high temperatures. At the same time, it was found that the CO gas concentration affected the sensitivity in the measurements performed by changing the CO concentration. It is believed that the samples can be used commercially in gas sensor applications.

Author contributions

FS contributed to investigation, data curation, methodology, IKE contributed to investigation, data curation, methodology, and resources. EY contributed to data curation, conceptualization, and resources. SA contributed to writing–review and editing, supervision, conceptualization, and methodology.

Funding

Open access funding provided by the Scientific and Technological Research Council of Türkiye (TÜBİTAK). This project was supported by the scientific research unit of Canakkale Onsekiz Mart University with the project code FHD-2023-4377.

Data availability

The data and materials that support our published claims stand well with the field standards and journal policies.

Code availability

Not applicable.

Declarations

Conflict of interest The authors declare no competing interests and all co-authors have approved the contents of this manuscript and submission.

Ethical approval Not applicable.

Consent for publication Not applicable.

References

1. I. Karaduman, M.A. Yıldırım, S.T. Yıldırım, A. Ateş, Y.A. Özdemir, S. Acar, J. Mater. Sci. Mater. Electron. **28**, 18154–18163 (2017)
2. J.-H. Kim, I. Sakaguchi, S. Hishita, T. Ohsawa, T.T. Suzuki, N. Saito, Sens. Actuators B Chem. **382**, 133501 (2023)
3. M.M. Can, M. Coşkun, T. Fırat, J. Alloys Compd. **542**, 241 (2012)
4. L.G. da Trindade, G. Yuji Hata, J. Carneiro Souza, M.R.S. Soares, E.R. Leite, E.C. Pereira, E. Longo, T.M. Mazzo, J. Mater. Sci. **55**, 2923–2936 (2020)
5. I. Irshad, A.G. Lone, B. Want, J. Alloys Compd. **971**, 172696 (2024)
6. Y. Zhao, C. Deng, D. Tang, L. Ding, Y. Zhang, H. Sheng, H. Ji, W. Song, W. Ma, C. Chen, J. Zhao, Nat. Catal. **4**, 684 (2021)
7. B. Iandolo, B. Wickman, I. Zorić, A. Hellman, J. Mater. Chem. A **3**, 16896 (2015)
8. M. Hjiri, S. Algessair, R. Dhahri, A. Mirzaei, G. Neri, RSC Adv. **14**, 17526 (2024)
9. B.K. Jha, S. Chaule, J. Jang, Mater. Chem. Front. **8**, 2197 (2024)
10. S. Saleem, N. Muhammad Ashiq, S. Manzoor, J. Mater. Res. Technol **25**, 6150–51 (2023)
11. A. Tsyganok, P. Monroy-Castillero, Y. Piekner, A. Yochelis, A. Rothschild, Energy Environ. Sci. **15**, 2445 (2022)
12. Y. Li, J. Dang, Y. Ma, H. Ma, Molecules **28**, 2035 (2023)
13. S. Li, X. Zhang, P. Zhang, G. Song, L. Yuan, Nanomaterials **12**, 2783 (2022)
14. X. Sun, Y. Yan, M. Kang, W. Zhao, K. Yan, H. Wang, R. Li, S. Zhao, X. Hua, B. Wang, W. Zhang, Y. Deng, Nat. Commun. **15**, 3870 (2024)
15. P. Shi, J. Xu, I. Yavuz, T. Huang, S. Tan, K. Zhao, X. Zhang, Y. Tian, S. Wang, W. Fan, Y. Li, D. Jin, X. Yu, C. Wang, X. Gao, Z. Chen, E. Shi, X. Chen, D. Yang, J. Xue, Y. Yang, R. Wang, Nat. Commun. **15**, 2579 (2024)
16. J. Tan, J. Wang, Q. Cao, H. Bi, J. Wu, X. Wang, Vacuum **212**, 112034 (2023)
17. Y.W. Phuan, M.N. Chong, T. Zhu, S. Yong, E.S. Chan, Mater. Res. Bull. **69**, 71 (2015)
18. Y. Caglar, S. Ilican, M. Caglar, F. Yakuphanoglu, J. Wu, K. Gao, P. Lu, D. Xue, J. Alloys Compd. **481**, 885 (2009)
19. A.H. Farahmand-Dashtarjandi, A. Yourdkhani, R. Poursalehi, N.B. Simhachalam, J. Alloys Compd. **962**, 171122 (2023)
20. A. Demircioğlu, K.Ç. Demir, J. Electron. Mater. **50**, 2750 (2021)
21. C. Wang, L. Guo, M. Lei, C. Wang, X. Chu, F. Yang, X. Gao, H. Wamg, Y. Chi, X. Yang, Nanomaterials **12**, 2397 (2022)
22. C. Muiva, D.P. Sebuso, E. Muchuweni, Physica B **690**, 416206 (2024)
23. T.C. Paul, J. Podder, M.H. Babu, Surf. Interfaces **21**, 100725 (2020)
24. S.A. Hassanzadeh-Tabrizi, Precise calculation of crystallite size of nanomaterials: review. J. Alloys Compd. **968**, 171914 (2023)
25. K. Lefatshe, G.T. Mola, C.M. Muiva, Heliyon **6**(6), e04186 (2020)
26. L.K. Dintle, P.V.C. Luhanga, C. Moditswe, C.M. Muiva, Physica E **99**, 91–97 (2018)
27. K.V. Chandekar, M. Shkir, A. Khan, S. AlFaify, Mater. Sci. Semicond. Process. **118**, 105184 (2020)
28. A. Badawi, S.S. Alharthi, A.A. Alotaibi, Appl. Phys. A **129**, 339 (2023)
29. D.A. Mazón-Montijo, D. Cabrera-German, A.S. Sánchez-Ovando, O.Y. Ramírez, Z. Esquivel Montiel-González, Opt. Mater. **110**, 110496 (2020)
30. M.F. Al-Kuhaili, M. Saleem, S.M.A. Durrani, J. Alloys Compd. **521**, 178 (2012)
31. J.Q. Chen, Q.S. Huang, R.Z. Qi, Nucl. Sci. Technol. **30**, 107 (2019)
32. H. Sun, Z. Xu, D. Zhang, Appl. Surf. Sci. **614**, 156202 (2022)
33. A. Šuligoj, D. Grinberg, Y. Paz, J. Phys. Chem. C **125**, 28013 (2021)
34. D.A. Grave, N. Yatom, D.S. Ellis, M.C. Toroker, A. Rothschild, Adv. Mater. **30**, 1706577 (2018)
35. S. Tekin, I. KaradumanEr, The structural, morphological, optical and gas-sensing properties of Mn_3O_4 thin films grown by successive ionic layer adsorption and reaction technique. J. Mater. Sci. Mater. Electron. **33**, 14519–14534 (2022)
36. L.C. Nehru, M. Umadevi, C. Sanjeeviraja, Int. J. Mater. Eng. **2**(1), 12–17 (2012)
37. H. Zhong, F. Pan, S. Yue, Phys. Chem. Lett. **14**, 6702 (2023)
38. J.A. Glasscock, P.R.F. Barnes, I.C. Plumb, M.A. Bendavid, Thin Solid Films **516**, 1716 (2008)
39. M. Shoorangiz, L. Shariatifard, H. Roshan, A. Mirzaei, Inorg. Chem. Commun. **133**, 108961 (2021)

40. M. Chakraborty, A. Ghosh, R. Thangavel, K. Asokan, J. Alloys Compd. **664**, 682 (2016)
41. A.N. Simões, G.M.M.M. Lustosa, E. de Souza Morita, A. Nunes de Souza, F. Torres, W.A. Bizzo, T. Mazon, Mater. Chem. Phys. **311**, 128576–77 (2024)
42. R. Xie, J. Lu, J. Wang, J. Ind. Eng. Chem. **131**, 248–256 (2024)
43. D. Zhang, Y. Sun, C. Jiang, Y. Yao, D. Wang, Y. Zhang, Sens. Actuators B **253**, 1120–1128 (2017)
44. Ö. Barin, A. Ajjaq, A.O. Çağırtekin, I. Karaduman Er, M.A. Yıldırım, A. Ateş, S. Acar, Sens. Actuators B **371**, 132499 (2022)
45. F. Xu, C. Zhou, H.-P. Ho, J. Alloys Compd. **858**, 158294 (2021)
46. Z. Tao, Y. Li, B. Zhang, G. Sun, M. Xiao, H. Bala, J. Cao, Z. Zhang, Y. Wang, Sens. Actuators B Chem. **298**, 126889 (2019)
47. B. Altun, I. Karaduman Er, A.O. Çağırtekin, A. Ajjaq, F. Sarf, S. Acar, Appl. Phys. A **127**, 687 (2021)
48. S. Tekin, I. Karaduman Er, J. Mater. Sci. Mater. Electron. **33**, 14519–14534 (2022)
49. F. Sarf, Metal oxide gas sensors by nanostructures, in *Gas Sensors* (Intech Open Horizons Publishing Company, London, 2020), pp. 1–18.
50. S. Sarıtaş, G.M. Muğlu, E. Turgut, M. Kundakçı, Md. Yıldırım, V. Şenay, Physica B **677**, 415704 (2024)
51. S. Lee, S. Choi, S.H. Park, Sens. Actuators B **395**, 134519 (2023)
52. H. Hao, D. Sun, Y. Xu, J. Colloid Interfaces Sci. **462**, 315 (2016)
53. S. Abbas, W. Yi, S. Yoo, A. Khalid, Z. Bhalli, J. Si, X. Hou, Phys. Status Solidi A **219**, 2100529 (2022)
54. Y. Hu, O.K. Tan, J.S. Pan, H. Huang, W. Cao, Sens. Actuators B **108**, 244 (2005)
55. R. Molavi, M.H. Sheikhi, Mater. Sci. Semicond. Process. **106**, 104767 (2020)
56. B. Aydas, A. Atılgan, A. Ajjaq, S. Acar, M.F. Öktem, A. Yildiz, Ceram. Int. **50**(18A), 32477–32489 (2024)
57. Y.F. Sun, S.B. Liu, F.L. Meng, J.Y. Liu, Z. Jin, L.T. Kong, J.H. Liu, Sensors **12**(3), 2610–2631 (2012)
58. C. Montoro, J.-Y. Kim, A. Mirzaei, J.-H. Lee, S. Sayegh, E. Makhoul, I. Iatsunskyi, E. Coy, M. Bechelany, H. WooKim, S. SubKim, Composites Part B Eng. **283**, 111637 (2024)
59. H.-J. Kim, J.-W. Yoon, K.-I. Choi, H. Won Jang, A. Umar, J.-H. Lee, Nanoscale **5**, 7066 (2013)
60. M. Wusiman, F. Taghipour, Crit. Rev. Solid State Mater. Sci. **47**(3), 416–435 (2022)
61. T. Thomas, Y. Kumar, J.A.R. Ramón, V. Agarwal, S.S. Guzmán, R. Reshmi, S. Pushpan, S.L. Loredo, K.C. Sanal, Vacuum. **184**, 109983 (2021)
62. L. Zhang, F.-C. Tian, X.-W. Peng, X. Yin, Sens. Actuators A **205**, 170–176 (2014)
63. V. Najafi, S. Zolghadr, S. Kimiagar, Optik **182**, 249–256 (2019)
64. X. Zhao, D. Shen, W.W. Duley, C. Tan, Y.N. Zhou, Adv. Energy Sustain. Res. **3**, 2100196 (2022)
65. X. Wang, Q. Zhang, Powder Technol. **371**, 55 (2020)
66. R. Dridi, I. Saafi, A. Mami, A. Amlouk, M. Amlouk, Surf. Interfaces **21**, 100743 (2020)
67. M. Nosonovsky, B. Bhushan, Multiscale effects and capillarity interactions in functional biomimetic surfaces for sustainability. Nano Today **3**(1–2), 53–65 (2008)
68. D. Quéré, Annu. Rev. Mater. Res. **52**, 491–513 (2022)
69. W. Li, M. Chen, P. Zhou, Y.Q. Wang, J. Mater. Chem. A **9**(10), 5895–5904 (2021)